Supplementary Information for

Resistance to the "Last Resort" Antibiotic Colistin: A Single-Zinc Mechanism for Phosphointermediate Formation in MCR Enzymes

Emily Lythell[a,b‡], Reynier Suardiaz[a,c,d,e†‡], Philip Hinchliffe[b‡], Chonnikan Hanpaibool[f], Surawit Visitsatthawong[g], A. Sofia F. Oliveira[a,c], Eric J. M. Lang[a], Panida Surawatanawong[g], Vannajan Sanghiran Lee[h], Thanyada Rungrotmongkul[f,i], Natalie Fey[a], James Spencer*[b], Adrian J. Mulholland*[a]

[a]*Centre for Computational Chemistry, School of Chemistry, University of Bristol, Cantock's Close, Bristol, BS8 1TS, UK.*
[b]*School of Cellular and Molecular Medicine, University of Bristol, University Walk, Bristol, BS8 1TD, UK.*
[c]*School of Biochemistry, University of Bristol, University Walk, Bristol, BS8 1TD, UK.*
[d]*Centre for Enzyme Innovation, School of Biological Sciences, Institute of Biological and Biomedical Sciences, University of Portsmouth, Portsmouth PO1 2DT, UK*
[e]*Department of Physical Chemistry, Faculty of Chemistry, Complutense University of Madrid, 28040 Madrid, Spain*
[f]*Structural and Computational Biology Research Unit, Department of Biochemistry, Faculty of Science, Chulalongkorn University, Bangkok 10330, Thailand*
[g]*Department of Chemistry and Center of Excellence for Innovation in Chemistry, Faculty of Science, Mahidol University, Bangkok 10400, Thailand*
[h]*Department of Chemistry, Faculty of Science, University of Malaya, Kuala Lumpur 50603, Malaysia*
[i]*Bioinformatics and Computational Biology Program, Graduate School, Chulalongkorn University, Bangkok 10330, Thailand*

Supplementary Information Table of Contents

Materials and Methods

Crystallisation and structure determination

The MCR-2 catalytic domain (MCR-2 residues 217–538, MCR-2CD) was expressed and purified as previously described[1], except for the final gel filtration step in which protein was loaded onto a Superdex 75 size-exclusion column equilibrated in 10 mM $NaPO_4$ pH 7.0. MCR-2CD eluted as a monomer and peak fractions were concentrated to 15 mg mL^{-1} by centrifugation. Crystallization screens were conducted in MRC 2-drop 96-well sitting drop plates at 19 °C, with diffraction quality crystals obtained in the JCSG-plus commercial screen (Molecular Dimensions) by mixing 0.2 µL protein solution with 0.2 µL reservoir solution (0.15 M KBr, 30% PEG2000MME) and equilibrating against 80 µL reservoir solution. Crystals were harvested in reservoir plus 25% glycerol and subsequently flash-cooled in liquid nitrogen. X-ray data were collected at 100K on beamline I24 at Diamond Light Source, integrated in Mosflm[2] and scaled and merged using AIMLESS[3] in the CCP4 suite.[4] Crystallographic phases were solved using Phaser[5] with MCR-2CD (PDB 5MX9)[1] as the starting model. The model was completed by iterative rounds of manual model building in Coot[6] and refinement in Phenix,[7] with structure validation assisted by MolProbity[8] and Phenix. Atomic coordinates and structure factors have been deposited in the Protein Data Bank (PDB 6SUT).

Molecular Dynamics Simulations

A flexible loop (residues 414 to 424) not modelled in the dizinc 5LRM crystal structure was rebuilt using Ramachandran-based loop fitting in Coot (version 0.8.8)[9]. Metal ion coordinates from dizinc structures were combined with apo-5LRN/6SUT structures (with phosphorylated Thr285) to model phosphorylated dizinc MCR-1/-2. The AmberTools17 program LEaP was used to protonate ionisable residues as determined by their predicted pKa values at pH 7.5 using PROPKA-3.1 (version 2.0.0)[10] and created a water shell of thickness of 5.0 Å using 8 multivariate Gaussians. The water shell was extended to a truncated octahedron of radius 10.0 Å using the TIP3P water model[11] with Na^+ and Cl^- ions added to a final concentration of 0.1 M after charge neutralisation. Parameter files for unprotonated phosphothreonine ('T2P') were obtained from the Bryce group database (University of Manchester).[12] Zinc ions were parameterised using the standard 12-6 Lennard-Jones (LJ) nonbonded model. MD was performed using the Amber ff14SB force field.

Minimisation was carried out in four stages; first restraining everything except the solvent, then backbone atoms only, then Cα atoms only, and finally without restraints. Zinc ions and their coordinating residues were restrained (25.0 kcal mol^{-1} $Å^2$) throughout minimisation, heating, and equilibration in order to prevent premature dissociation of the metal. The system was minimised for 1,000 cycles using the method of steepest descent, followed by the conjugate gradient method up to a total 10,000 cycles for each stage. Long-range Van der Waals interactions were truncated using a 10.0 Å cut-off.[13] The system was heated from 10.0 K to 298.0 K over 200 ps with a 2 fs timestep, using Langevin dynamics with collision frequency γ = 5.0 ps^{-1}. Constant volume periodic boundaries and SHAKE constraints were used. Equilibration at 298.0 K was performed in four 500 ps stages, restraining as before. Langevin dynamics were used with collision frequency γ = 2.0 ps^{-1}. The system was equilibrated at a constant pressure of 1.01325 bars (~1 atm) using the Berendsen barostat, with a relaxation time of 1.0 ps. Production MD runs were performed for each system for a minimum of three 100 ns runs for MCR-1 and two 100 ns runs for MCR-2.

DFT cluster modelling

Starting geometries for the cluster model were based on the X-ray structure of the MCR-1 extracellular domain as previously reported (PDB: 5LRN).[14] This structure contains one Zn atom tetra-coordinated to phosphorylated Thr285, Glu246, Asp465 and His466. All these residues were included in the active site model as well as the His395 and His478 residues, see Figure 4. To reduce the size of the model, amino acids were truncated at Cα, so that only side chains were kept in the model. In order to represent the physiological substrate (phosphatidylethanolamine) and product (phosphoethanolamine bound to Thr285) methyl groups were added to the phosphate to represent phosphoethanolamine and the departing phosphoethanolamine moiety. Hence phosphatidylethanolamine is here represented as dimethyl phosphate. Oxygen positions of the Thr285-bound phosphoryl group in the crystal structure were used as a guide for starting geometry for transition state (TS) calculations. Reactant and product states were subsequently obtained from TS final geometry. All Cα atoms were kept frozen in their positions as defined in the crystal structure during DFT calculations to preserve the approximate spatial arrangement of the active site residues.

Calculations were performed by using the B3LYP functional[15] as implemented in the Gaussian 09 package.[16] Dispersion corrections were included using the B3LYP-GD3BJ method (D3 version of Grimme's dispersion with Becke-Johnson damping).[17, 18] A combination of the 6-31+G(d,p) basis set for the phosphorus and the oxygens

coordinated to Zn, SDD Stuttgart/Dresden effective core potential for Zn and 6-31G(d) basis set for the rest of the atoms, was used. Solvation effects were evaluated by single-point calculations on the optimized geometries at the same level of theory as the geometry optimizations using the conductor-like polarized continuum model (C-PCM)[19] and ε = 4, as widely used in DFT cluster model calculations of enzymes.[20, 21] Additional single point calculations using ε from 3 to 15 were performed to confirm that the energetics are not very sensitive to ε (see Supplementary Information). Frequency calculations were performed at the same level of theory as the geometry optimizations to obtain free energy corrections at 298.15 K and 1 atm pressure as well as to confirm the nature of the stationary points. Some imaginary frequencies occur in the stationary points due to the frozen atoms in the model, but these are small and confined to the vicinity of the frozen atoms.

Table S1. Zinc Coordination Distances in Crystal Structures of MCR-1 and MCR-2.

Crystal structure distances			Distance (Å)			
			MCR-1		MCR-2	
	Residue	Atom	5LRN[14]	5LRM[14]	6SUT	5MX9[1]
Zn1	Glu246	OE1	2.55	2.62	2.53	2.57
		OE2	1.91	2.04	1.83	1.92
	His466	NE2	2.07	2.10	2.13	2.04
	Asp465	OD1	2.00	1.99	2.05	1.92
	Thr285	OG1	2.35	2.10	1.91	1.92
		O2P	2.12	N/A	2.35	N/A
Zn2	His395	NE2	N/A	1.87	N/A	2.00
	His478	NE2	N/A	2.04	N/A	1.93

Table S2: Crystallographic Data Collection and Refinement Statistics for Monozinc (phospho-Thr285) MCR-2

Data collection	
PDB id	6SUT
Beamline	DLS I24
Space group	$P2_12_12_1$
Molecules/ASU	1
Cell dimensions	
a, *b*, *c* (Å)	43.08, 53.57, 122.67
α, β, γ (°)	90.0, 90.0, 90.0
Wavelength (Å)	0.911
Resolution (Å)*	53.57 – 1.20 (1.22 – 1.20)
R_{pim}	0.034 (0.426)
$CC_{1/2}$	0.998 (0.623)
I / σ(I)	11.7 (2.3)
Completeness (%)	98.1 (96.9)
Redundancy	10.0 (9.5)
Refinement	
Resolution (Å)	49.09 – 1.20
No. reflections	87,699
R_{work} / R_{free}	0.1411 / 0.1538
No. non-H atoms	
Protein	2590
Solvent	469
Zinc ions	1
B-factors	
Protein	14.31
Solvent	27.30
Zinc ions	15.62
R.m.s. deviations	
Bond lengths (Å)	0.008
Bond angles (°)	0.960
Ramachandran (%)	
Outliers	0.31
Favoured	98.12

*Values in parentheses are for highest-resolution shell.

Table S3. Zn1 Coordination by Glu246 and Asp465 Side Chain Carboxylates.

		Average distance (Å) to Zn1 ± one S.D.							
		Monozinc MCR-1		Monozinc MCR-2		Dizinc MCR-1		Dizinc MCR-2	
		Crystal (5LRN)	Simulation (300 ns)	Crystal (6SUT)	Simulation (200 ns)	Crystal (5LRM)	Simulation (300 ns)	Crystal (5MX9)	Simulation (200 ns)
Monodentate Glu246	OE1	2.55	2.98 ± 0.15	2.53		2.62	**3.4 ± 0.18**	2.57	3.3 ± 0.16
	OE2	1.91	1.76 ± 0.04	1.83		2.04	**1.75 ± 0.04**	1.92	1.83 ± 0.05
	% of simulation*		35.3%*				**99.0%**		26.0%
Bidentate Glu246	OE1		**1.88 ± 0.07**		**1.94 ± 0.15**		1.81 ± 0.05		**1.82 ± 0.05**
	OE2		**1.82 ± 0.05**		**1.81 ± 0.05**		1.87 ± 0.07		**1.75 ± 0.04**
	% of simulation*		**64.7%**		**100%**		1.0%		**74.0%**
Monodentate Asp465	OD1	2.00	**1.83 ± 0.06**	2.05	**1.75 ± 0.04**	1.99		1.92	3.16 ± 0.13
	OD2	3.06	**3.07 ± 0.4**	3.30	**2.81 ± 0.27**	2.99		2.95	1.76 ± 0.01
	% of simulation*		**80.3%**		**73.9%**				0.3%
Bidentate Asp465	OD1		1.76 ± 0.04		1.80 ± 0.05		**1.84 ± 0.06**		**1.87 ± 0.07**
	OD2		1.87 ± 0.07		1.99 ± 0.10		**1.81 ± 0.05**		**1.80 ± 0.05 (199.5 ns)**
	% of simulation*		19.7%		26.1%		**100.0%**		**99.8%**

*Percentages represent the coverage of conformational space sampled over the simulations.
Tabulated values are averages over single MD trajectories of the durations shown. Figures in bold represent values for Zn1/Zn2 coordination in the dominant population for a given trajectory.

Table S4. DFT Calculation of Reaction Energies and Barriers for PEA Transfer to Thr285

		One Zn^{2+} ion			Two Zn^{2+} ions
		Histidine protonation			
Reaction pathway		None	His395 only	His395, His478	None
A	$\Delta G^{‡}$		20.3	10.2	33.5
	ΔG		-5.0	-11.5	17.0
B	$\Delta G^{‡}$	41.2			
	ΔG	8.7			

$\Delta G‡$: calculated barriers (kcal/mol)
ΔG: reaction energies (kcal/mol)

Note that mechanisms with Thr285 deprotonated were also investigated, but discarded due to an inability to locate an appropriate transition state.

Table S5. Reaction Barrier Heights ($\Delta E^{\ddagger}$) and Reaction Energies (ΔE) Calculated at Different Values of Dielectric Constants from Single Point (sp) Energy Calculations.

Single point calculations were carried out at a range of dielectric constants (ε) for the favoured reaction pathway (Pathway A) for mono-zinc MCR-1 (Figure 3), with geometries optimised at the B3LYP-D3 level, to check the sensitivity of reaction barrier height ($\Delta E^{\ddagger}$) and energy of reaction (ΔE) to this property. Small variations (< 2.5 kcal/mol) in were found for $3 < \varepsilon < 15$. Since, typically, the effect of ε on DFT cluster model calculations saturates with the size of the system[22], we consider this small cluster as appropriate in size.

	$\Delta E^{\ddagger}$	ΔE
(opt) vacuum	18.8	-1.1
(sp) ε=3	22.7	3.9
(sp) ε=4	23.4	4.7
(sp) ε=5	23.8	5.2
(sp) ε=6	24.2	5.6
(sp) ε=7	24.4	5.8
(sp) ε=8	24.6	6.0
(sp) ε=9	24.7	6.2
(sp) ε=10	24.9	6.3
(sp) ε=11	25.0	6.4
(sp) ε=12	25.0	6.5
(sp) ε=13	25.1	6.6
(sp) ε=14	25.2	8.5
(sp) ε=15	25.2	6.7

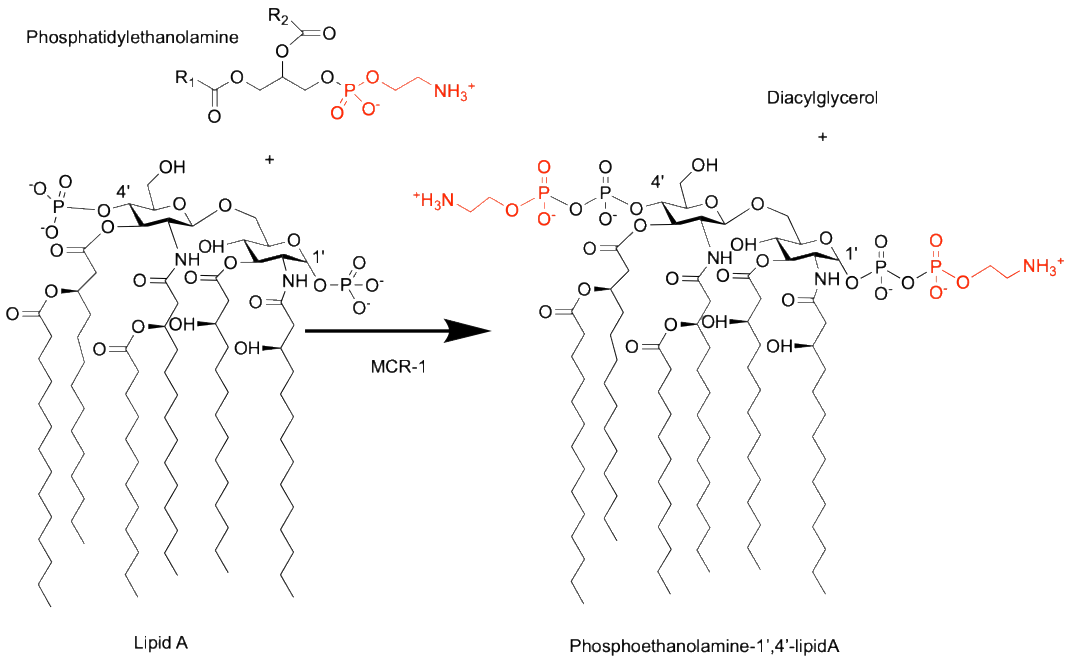

Figure S1. Reaction Scheme for Phosphoethanolamine (PEA) Transfer Catalysed by MCR Enzymes.

MCR-1 and -2 remove the charged PEA head-group (red) from the membrane-embedded phospholipid phosphatidylethanolamine, and transfer it to the 1' or 4' phosphates of lipid A to form either phosphoethanolamine-1' or 4'-lipid A.

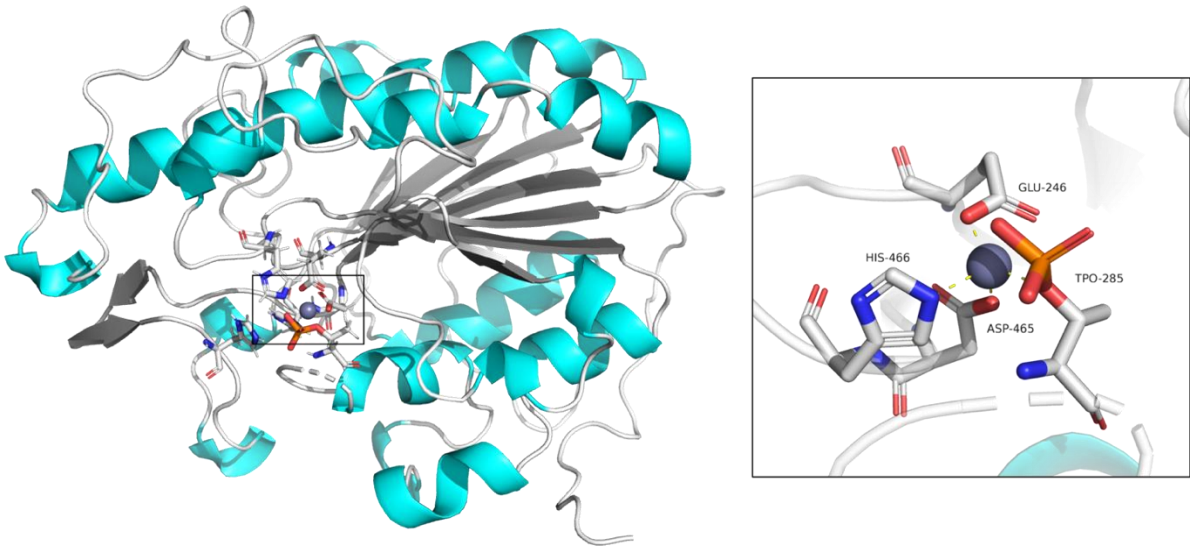

Figure S2. Crystal Structure of Mono-Zinc, Phosphorylated, MCR-2 Catalytic Domain

Cartoon representation of the mono-zinc phospho-Thr285 crystal structure presented in this study (PDB ID: 6SUT). Inset: Zn1 is coordinated by Glu246, His466, Asp465 and phospho-Thr285 (TPO-285, Oγ and OP atoms). Superposition onto our previous structure of phosphorylated MCR-1 (PDB 5LRN) gives overall C_α RMSD of 0.303 Å over 269 atoms, with alignment of the Zn1 coordinating residues Glu246, phosphoThr285, Asp465 and His466 giving all-atom RMSD of 0.073 Å over 18 atoms, confirming the active sites of MCR-1 and MCR-2 as virtually identical in the phosphorylated, as well as dephosphorylated, state.

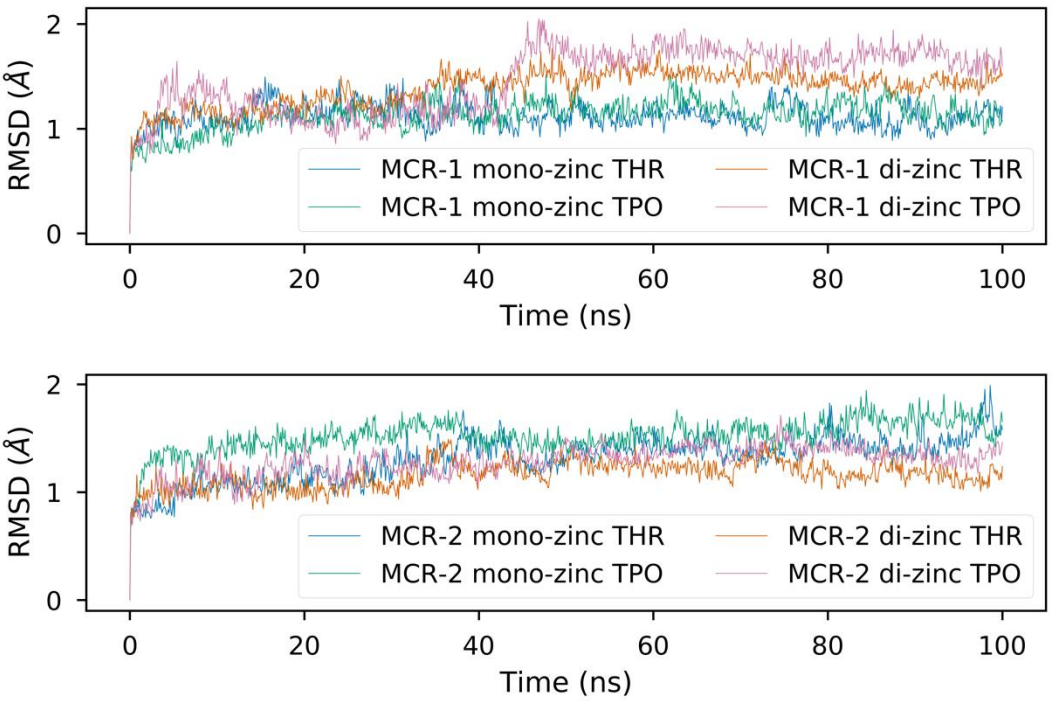

Figure S3. C_α RMSD Values for Molecular Dynamics (MD) Simulations of MCR Catalytic Domains

Global C_α RMSD values (Å) over the first 100 ns of MD simulations for MCR-1 and MCR-2 catalytic domains with reference to the equilibrated starting structure (frame 0). Each enzyme was simulated in mono- and di-zinc forms with Thr285 phosphorylated (TPO) and dephosphorylated (THR). Note that global RMSD remains <2.0 Å through each simulation,

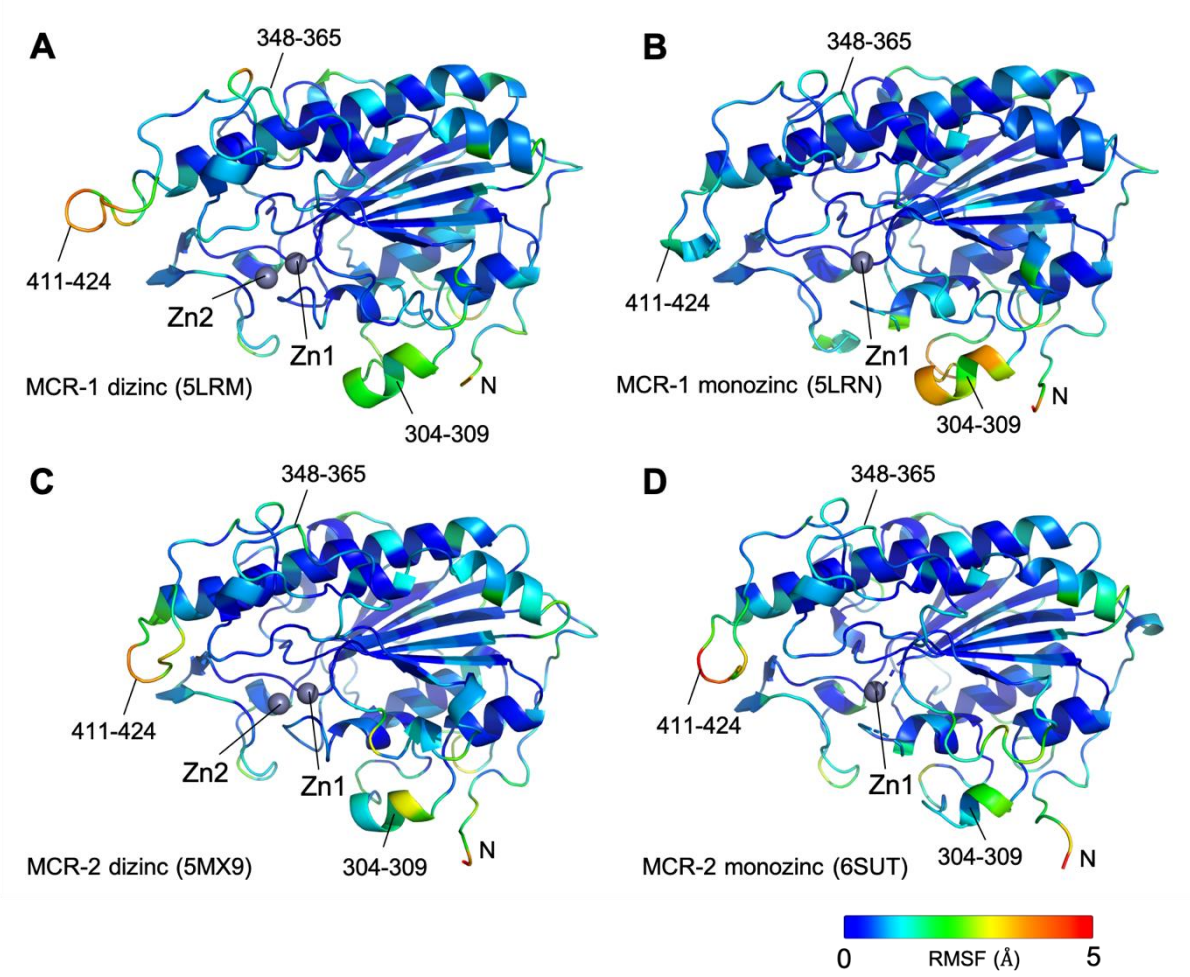

Figure S4. Stability of MCR-1 and MCR-2 During Extended Molecular Dynamics Simulations.

Cartoon representations of MCR-1 and MCR-2 crystal structures are coloured by RMSF (dark blue, low RMSF; red, high RMSF) calculated over 200 ns of MD simulation, with zinc ions shown as grey spheres. (A) MCR-1 dizinc structure 5LRM[14] (unmodified Thr285); (B) MCR-1 monozinc structure 5LRN[14] (phospho-Thr285); (C) MCR-2 dizinc structure 5MX9[1] (unmodified Thr285); (D): MCR-2 monozinc structure 6SUT (this work) (phospho-Thr285). Labels identify surface loops (residues 348-365 and 411-424), the α-helix formed by residues 304-309, the N-terminus, and zinc ions (grey spheres). Only small fluctuations in solvent exposed regions are seen, in particular including residues 411 – 424 (disordered in some crystal structures).

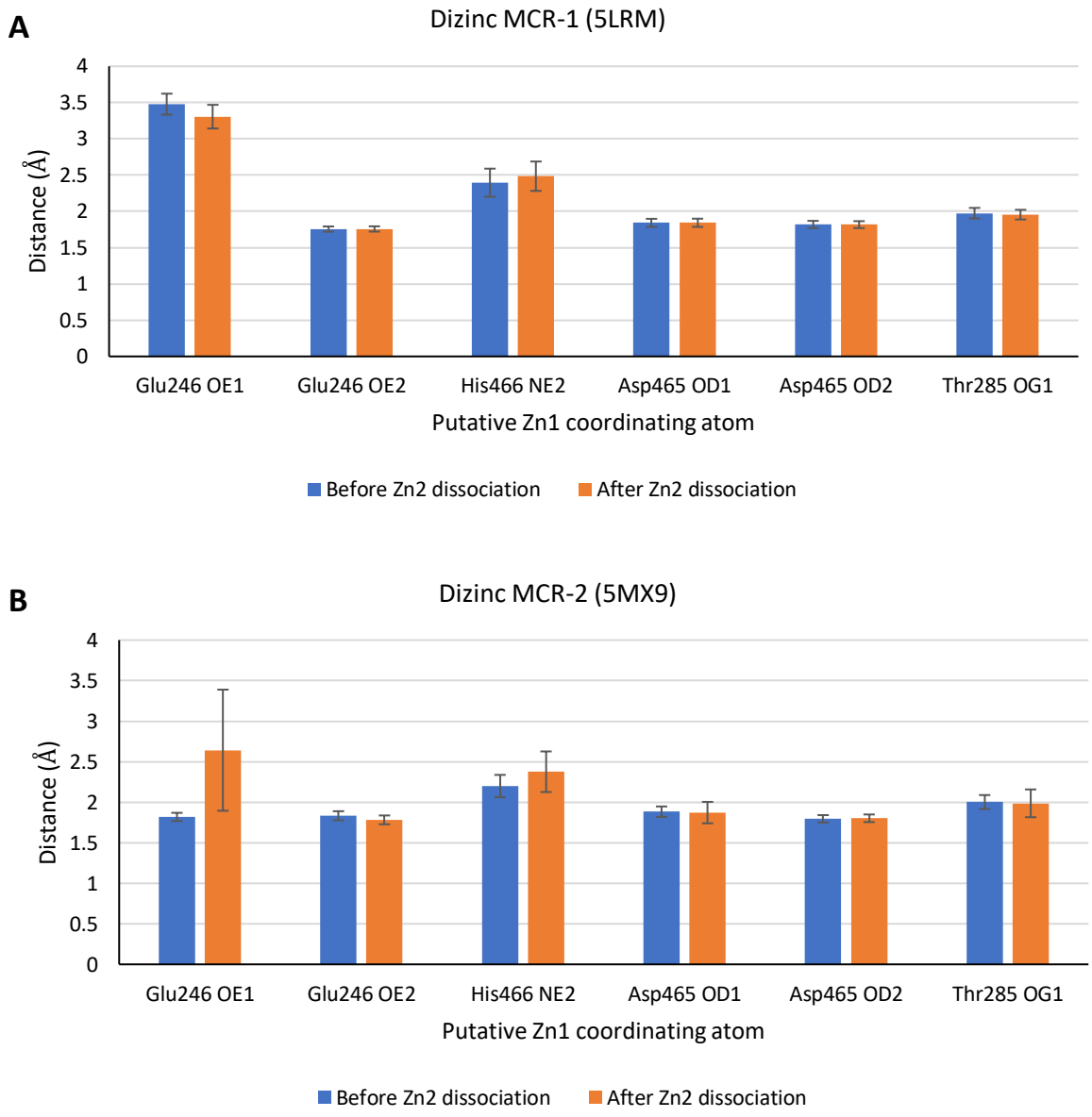

Figure S5. Effect of Zn2 Dissociation on MCR Zn1 Site Stability

Values calculated from representative simulations (single runs) **of the dephosphorylated resting enzyme**). **A.** Average MCR-1 Zn1 coordinating distances before (blue, simulation time up to 150 ns) and after (orange, simulation time 170 - 300 ns) dissociation of Zn2. Error bars show ± one standard deviation. The MCR-1 dizinc crystal structure (5LRM) was simulated for 300 ns. The Zn2 ion dissociated at ~160 ns and thereafter diffused freely in solution. RMSF values of Zn1 and Zn2 (before dissociation) were 5.0 Å and 9.9 Å, respectively, over 160 ns. After dissociation of Zn2 at 160 ns, the RMSF of Zn1 rose to 7.4 Å while that of Zn2 (calculated from the trajectory between 160 - 300ns) rose to 41.7 Å as it moved freely in solution. (In repeat simulations Zn2 dissociated after 1 ns of simulation or, in one simulation, dissociated at 40 ns and was then able to rebind to the Zn2 site at 200 ns, with coordination distances matching those of the pre-dissociated structure). **B.** Average MCR-2 Zn1 coordinating distances before (blue, up to 100 ns) and after (orange, 105 - 200 ns) dissociation of Zn2. Error bars show ± one standard deviation. The MCR-2 dizinc crystal structure (5MX9) was simulated for 200 ns. Zn2 was seen to dissociate at 103 ns and thereafter diffused freely in solution. (In repeat simulation Zn2 dissociated after 1 ns). RMSF values before Zn2 dissociation were 3.1 Å and 4.9 Å for Zn1 and Zn2, respectively, rising to 5.3 Å and 36.0 Å after Zn2 dissociation.

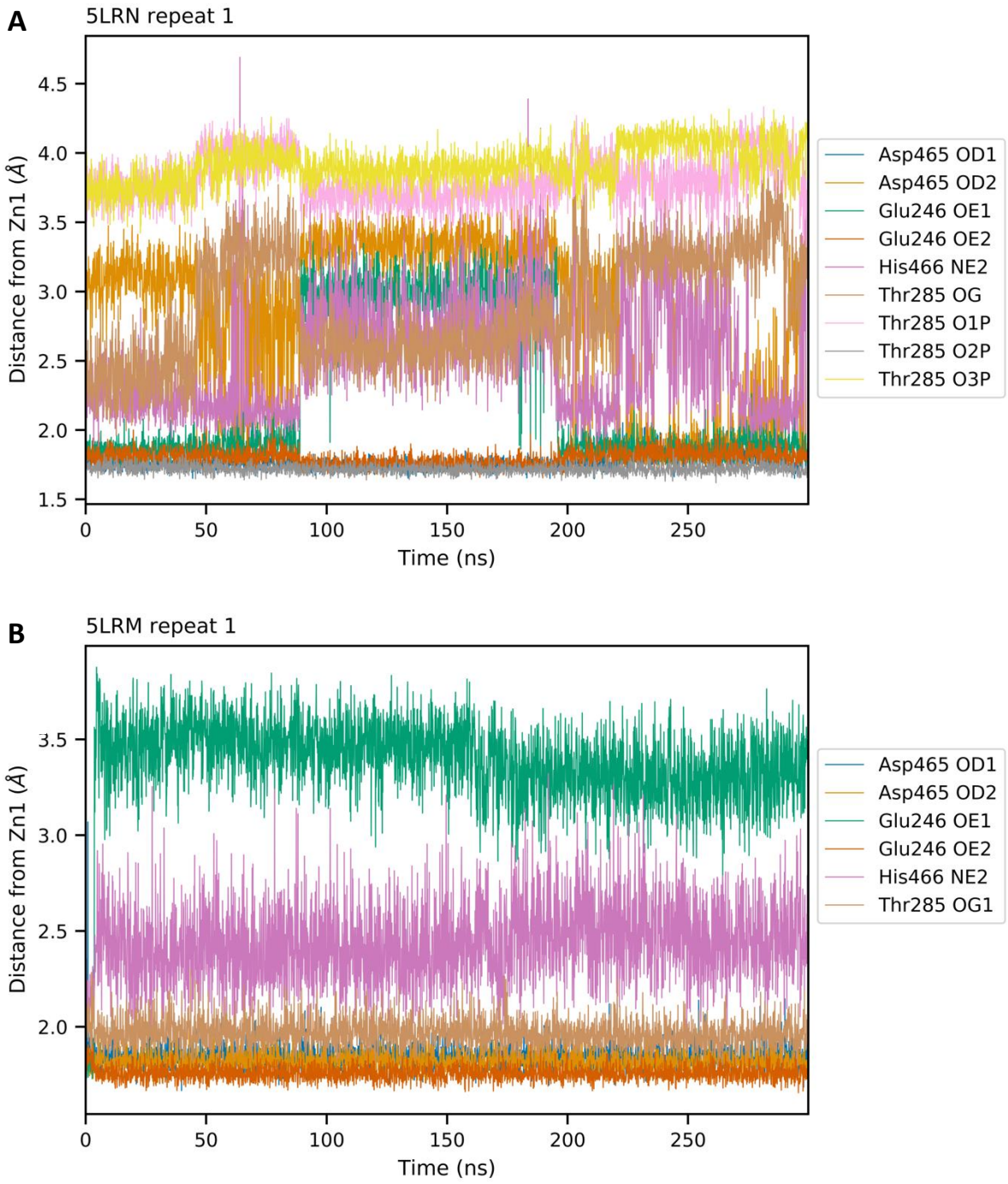

Figure S6. Zn1 Coordination for Monozinc (5LRN, A) and Dizinc (5LRM, B) MCR-1 Over 300 ns MD Simulation.

Time-dependence of distance from Zn1 zinc ion (measured from the geometric centre) to putative coordinating atoms over a single 300 ns MD simulation. Stepwise jumps in co-ordination distances represent exchange of individual residues between different stable rotamers (e.g. switch of Zn1 coordination by 5LRN Glu246 from bi- to monodentate between ~90 and 200 ns). See Table S3 for details of coordination distances and rotamer populations over time.

A. For monozinc MCR-1 (PDB 5LRN, Thr285 phosphorylated) both Glu246 and Asp465 form either mono- or bidentate coordination with Zn1. Glu246 makes monodentate coordination to Zn1 over 35.3% and bidentate coordination for the remaining 64.6% of the simulation. Asp465 makes monodentate coordination to Zn1 over

70.9% of the simulation, and bidentate coordination for the remaining 29.1%. Zn1 remains strongly coordinated by one of the phosphate oxygens (average 1.72 Å ± 0.03 over 300 ns) for the entire duration of the simulation. (Similar behaviour is observed for MCR-2 (phosphate oxygen – Zn1 distance 1.73 Å ± 0.03 over 200 ns)).

B. For dizinc MCR-1 (PDB 5LRM, Thr285 unmodified), Zn1 coordination by Thr285 Oγ is maintained at 1.97 Å ± 0.07 (calculated over the first 130 ns of the trajectory before dissociation of Zn2 at 150 ns) and 1.95 Å ± 0.07 (calculated over 170-300 ns of the trajectory after Zn2 dissociation), consistent with the distance measured in the crystal structure (2.10 Å).

In simulations of dizinc MCR-2 (PDB 5MX9, Thr285 unmodified, data not shown) equivalent distances measure 2.01 Å ± 0.15 (calculated over 100 ns before Zn2 dissociates) and 1.97 Å ± 0.11 (calculated over 100 ns after Zn2 dissociation), compared to the crystal structure distance of 1.92 Å.

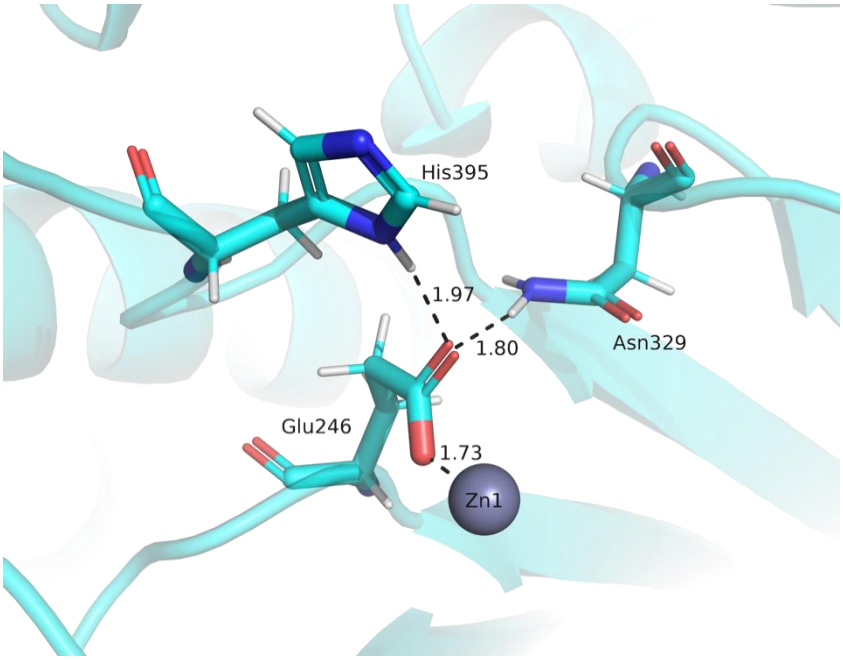

Figure S7. Second Shell Interactions of Glu246.

Representative frame (152.9 ns of a 300 ns trajectory) for MD simulation of monozinc MCR-1 (5LRN) showing monodentate coordination of Zn1 by Glu246 Oε2 (distance 1.73 Å). This rotamer is stabilised by hydrogen bonds from Glu246 Oε1 to Asn329 (Nδ2) and His395 (Nδ1). This network forms for the 35% of the 300 ns simulation when Glu246 makes monodentate coordination of Zn1. When present average hydrogen bond lengths are 2.00 Å ± 0.20 (Glu246 Oε1 - Asn329 Nδ2) and 2.17 Å ± 0.75 (Glu246 Oε1 - His395 Nδ1) respectively. Note that His395 coordinates Zn2 when present; in these circumstances Glu246 is stabilised solely by interactions with Asn329.

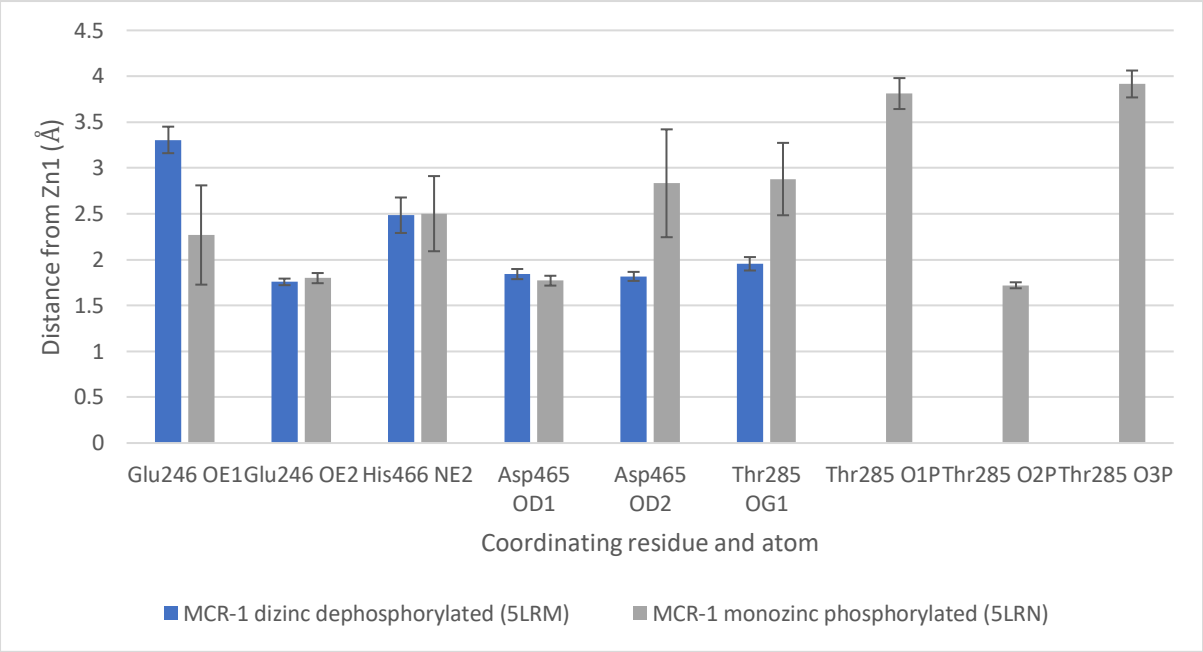

Figure S8. Effect of Thr285 Phosphorylation on Zn1 Site Architecture.

Comparison of Zn1 coordination over 150-300 ns of 300 ns trajectories for MD simulations of phosphorylated (5LRN) and dephosphorylated (5LRM) MCR-1. Note that Zn2 dissociated from the dephosphorylated enzyme after 140 ns of simulation, enabling comparison of the behaviour of the Zn1 site in two monozinc systems. Bars represent average distances with error bars ± one standard deviation.

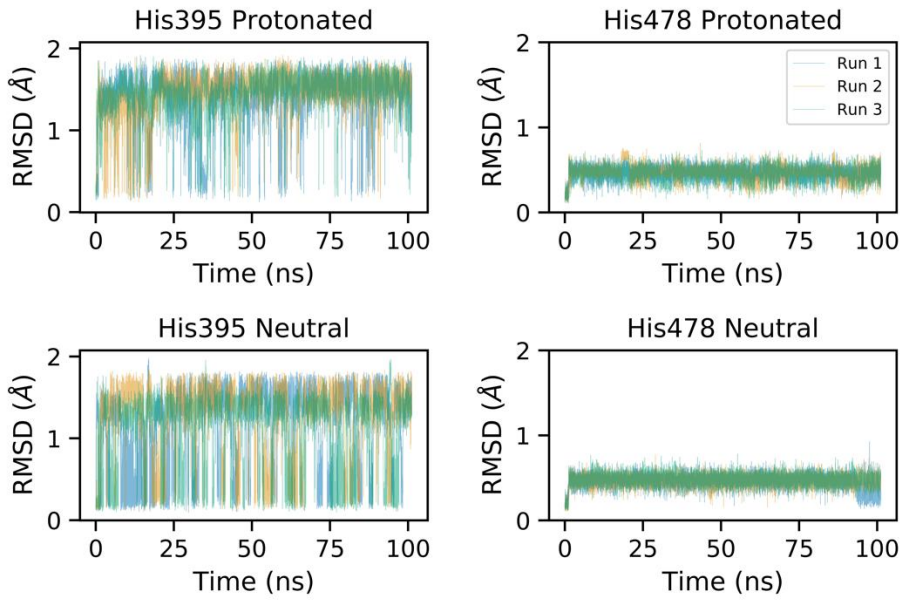

Figure S9: Effect of Protonation on Dynamics of His Residues in MCR Zn2 Site.

RMSD plots for His395 and His478 in protonated (top) and neutral (bottom) forms in unphosphorylated, mono-zinc MCR-1, over 100 ns MD simulations. Note the overall increase in RMSD on protonation of His395. Simulations (3 x 100 ns) of monozinc, dephosphorylated MCR-1 averaged Cα RMSD values (relative to the 5LRN starting structure) of 1.15 Å ± 0.5 and 0.47 Å ± 0.08 for neutral His395 and His478, respectively; and 1.42 Å ± 0.3 and 0.46 Å ± 0.08 when these residues were protonated.

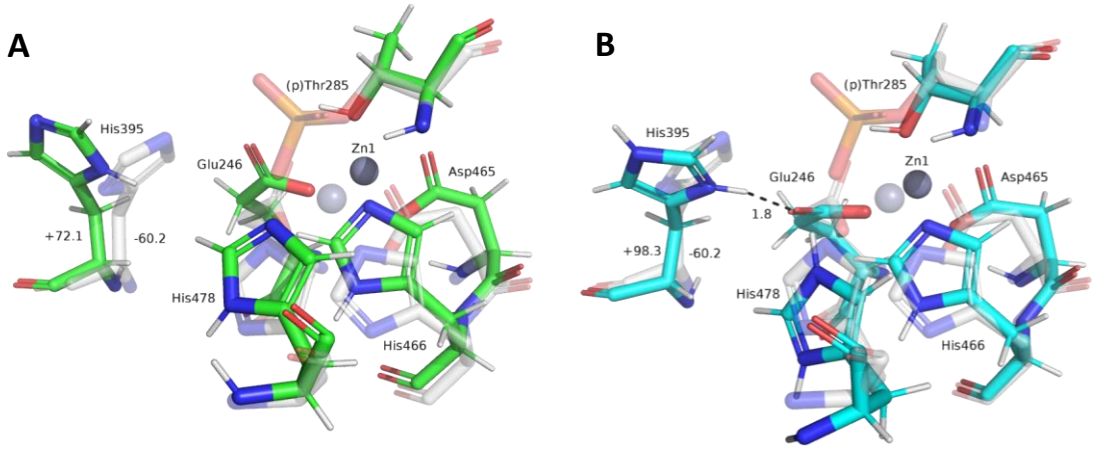

Figure S10: Effect of Protonation upon Conformations of MCR His395 and His478.

Figure shows superposition of active sites of monozinc, phosphorylated MCR-1 (pdb 5LRN[14], grey) and final snapshot of MD simulations for monozinc, dephosphorylated MCR-1 with His395/His478 neutral (A, left, green) or protonated (B, right, cyan). Side chain dihedral angles (χ2) for His395 are shown. During simulations the His395 χ2 dihedral (-60.2° in 5LRN) distributes between two distinct rotamers (for neutral His395average dihedrals -82.7° ± 29.0 (30%) and +76.9° ± 20.0 (70%)), shifting on protonation to average values of -97.3° ± 45.1 (10% populated) and +78.0° ± 18.0 (90%).

The χ2 dihedral angle around the His478 Cβ-Cγ axis (-86.7° in 5LRN) was unaffected by protonation, consistent with the presence of a strong hydrogen bond between His478 Nδ and the Glu468 side chain carboxylate.

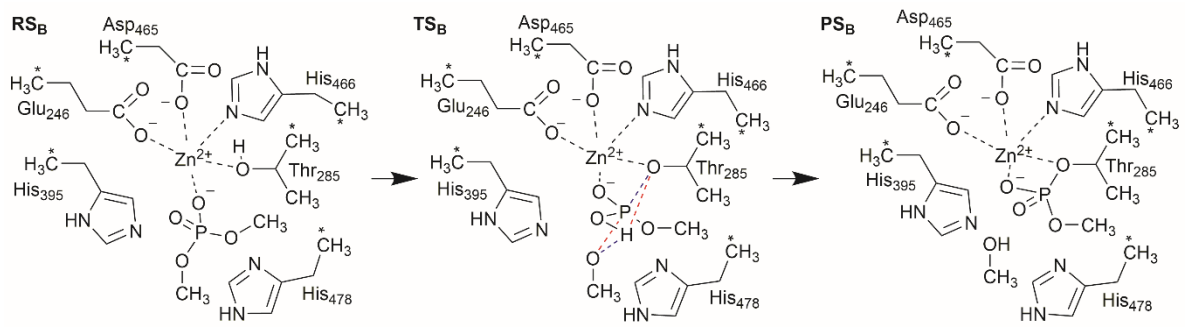

Figure S11. Second Potential Mechanism (Pathway B) for Phosphoethanolamine Transfer to Thr285.

Figure shows reactant (RS), transition (TS) and product (PS) states derived from DFT models for PEA transfer to Thr285 of monozinc MCR-1. PEA is represented as dimethyl phosphate (see Methods). Blue dashed lines represent bonds forming; red, bonds breaking. C_α atoms are marked with asterisks (*). This second pathway tested was found to be less energetically favourable than pathway A (Figure 4), calculated energies are presented in Table 1.

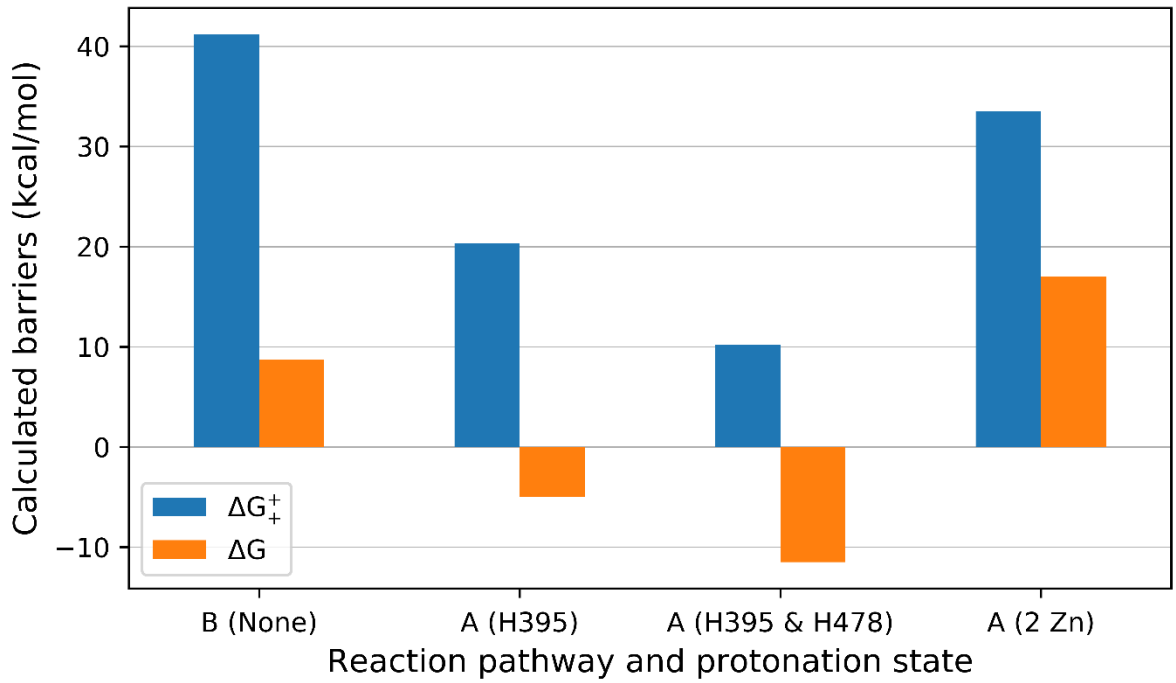

Figure S12: Reaction Barrier Heights (ΔE‡) and Reaction Energies (ΔE) for Alternative Pathways for Generation of MCR Phospho-Intermediate.
Barriers derived from DFT calculations for reaction pathways A (Figure 3) for mono-zinc MCR-1 with either His395, or both His395 and His478 protonated, or for di-zinc MCR-1; or for pathway B (Figure S11).

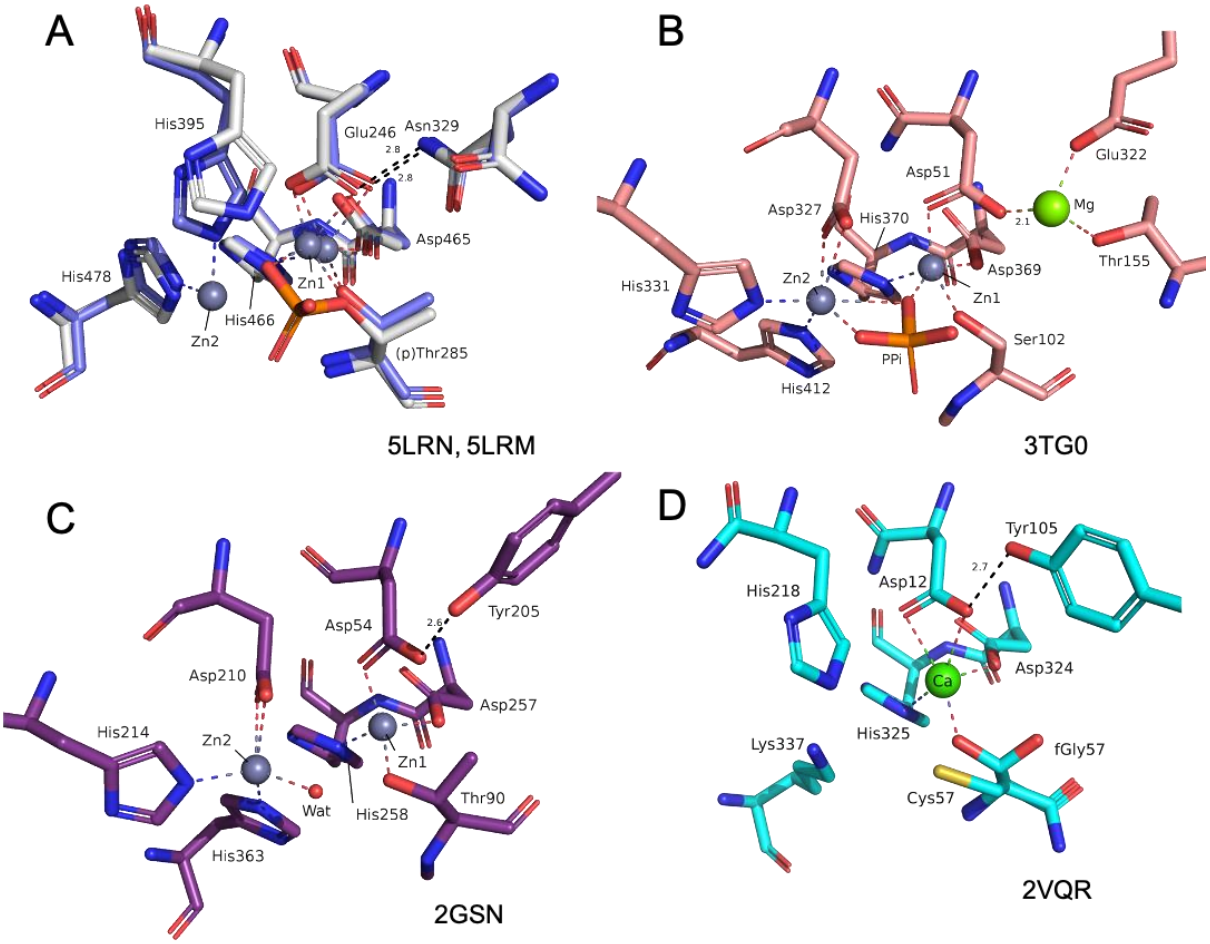

Figure S13: Active Sites of Alkaline Phosphatase Superfamily Members
Active sites for A. MCR-1 (mono-zinc (pdb 5LRN[14]) and di-zinc (pdb 5LRM[14]) forms. B. *Escherichia coli* alkaline phosphatase (AP, pdb 3TG0[23]). C. *Xanthomonas axonopodis pv. citri* nucleotide pyrophosphatase/phosphodiesterase (pdb 2GSN[24]). D. *Rhizobium leguminosarum* Phosphonate Monoester Hydrolase/Phosphodiesterase (PMH, pdb 2VQR[25]). Note presence of Mg^{2+} ion in AP active site, replaced by neutral residues (Asn329 Tyr205 Tyr105) in enzymes active against phosphodiester substrates, and mono-metallic active site of PMH.

Supplementary References

1. K. Coates, T. R. Walsh, J. Spencer and P. Hinchliffe, *Acta Crystallographica Section F*, 2017, **73**, 443-449.
2. T. G. Battye, L. Kontogiannis, O. Johnson, H. R. Powell and A. G. Leslie, *Acta Crystallogr D Biol Crystallogr*, 2011, **67**, 271-281.
3. P. R. Evans and G. N. Murshudov, *Acta Crystallogr D Biol Crystallogr*, 2013, **69**, 1204-1214.
4. M. D. Winn, C. C. Ballard, K. D. Cowtan, E. J. Dodson, P. Emsley, P. R. Evans, R. M. Keegan, E. B. Krissinel, A. G. Leslie, A. McCoy, S. J. McNicholas, G. N. Murshudov, N. S. Pannu, E. A. Potterton, H. R. Powell, R. J. Read, A. Vagin and K. S. Wilson, *Acta Crystallogr D Biol Crystallogr*, 2011, **67**, 235-242.
5. A. J. McCoy, R. W. Grosse-Kunstleve, P. D. Adams, M. D. Winn, L. C. Storoni and R. J. Read, *J Appl Crystallogr*, 2007, **40**, 658-674.
6. P. Emsley, B. Lohkamp, W. G. Scott and K. Cowtan, *Acta Crystallogr D Biol Crystallogr*, 2010, **66**, 486-501.
7. P. D. Adams, P. V. Afonine, G. Bunkoczi, V. B. Chen, I. W. Davis, N. Echols, J. J. Headd, L. W. Hung, G. J. Kapral, R. W. Grosse-Kunstleve, A. J. McCoy, N. W. Moriarty, R. Oeffner, R. J. Read, D. C. Richardson, J. S. Richardson, T. C. Terwilliger and P. H. Zwart, *Acta Crystallogr D Biol Crystallogr*, 2010, **66**, 213-221.
8. V. B. Chen, W. B. Arendall, 3rd, J. J. Headd, D. A. Keedy, R. M. Immormino, G. J. Kapral, L. W. Murray, J. S. Richardson and D. C. Richardson, *Acta Crystallogr D Biol Crystallogr*, 2010, **66**, 12-21.
9. P. Emsley, B. Lohkamp, W. G. Scott and K. Cowtan, *Acta Crystallographica Section D*, 2010, **66**, 486-501.
10. M. H. M. Olsson, C. R. Søndergaard, M. Rostkowski and J. H. Jensen, *Journal of Chemical Theory and Computation*, 2011, **7**, 525-537.
11. W. L. Jorgensen, J. Chandrasekhar, J. D. Madura, R. W. Impey and M. L. Klein, *The Journal of Chemical Physics*, 1983, **79**, 926-935.
12. N. Homeyer, A. H. C. Horn, H. Lanig and H. Sticht, *Journal of Molecular Modeling*, 2006, **12**, 281-289.
13. S. Piana, K. Lindorff-Larsen, R. M. Dirks, J. K. Salmon, R. O. Dror and D. E. Shaw, *PLOS ONE*, 2012, **7**, e39918.
14. P. Hinchliffe, Q. E. Yang, E. Portal, T. Young, H. Li, C. L. Tooke, M. J. Carvalho, N. G. Paterson, J. Brem, P. R. Niumsup, U. Tansawai, L. Lei, M. Li, Z. Shen, Y. Wang, C. J. Schofield, A. J. Mulholland, J. Shen, N. Fey, T. R. Walsh and J. Spencer, *Scientific Reports*, 2017, **7**, 39392.
15. A. D. Becke, 1993, **98**, 5648-5652.
16. M. J. Frisch, G. W. Trucks, H. B. Schlegel, G. E. Scuseria, M. A. Robb, J. R. Cheeseman, G. Scalmani, V. Barone, B. Mennucci, G. A. Petersson, H. Nakatsuji, M. Caricato, X. Li, H. P. Hratchian, A. F. Izmaylov, J. Bloino, G. Zheng, J. L. Sonnenberg, M. Hada, M. Ehara, K. Toyota, R. Fukuda, J. Hasegawa, M. Ishida, T. Nakajima, Y. Honda, O. Kitao, H. Nakai, T. Vreven, J. A. Montgomery, J. E. Peralta, F. Ogliaro, M. Bearpark, J. J. Heyd, E. Brothers, K. N. Kudin, V. N. Staroverov, R. Kobayashi, J. Normand, K. Raghavachari, A. Rendell, J. C. Burant, S. S. Iyengar, J. Tomasi, M. Cossi, N. Rega, J. M. Millam, M. Klene, J. E. Knox, J. B. Cross, V. Bakken, C. Adamo, J. Jaramillo, R. Gomperts, R. E. Stratmann, O. Yazyev, A. J. Austin, R. Cammi, C. Pomelli, J. W. Ochterski, R. L. Martin, K. Morokuma, V. G. Zakrzewski, G. A. Voth, P. Salvador, J. J. Dannenberg, S. Dapprich, A. D. Daniels, Farkas, J. B. Foresman, J. V. Ortiz, J. Cioslowski and D. J. Fox, *Journal*, 2009, DOI: citeulike-article-id:9096580.
17. S. Grimme, S. Ehrlich and L. Goerigk, *Journal of Computational Chemistry*, 2011, **32**, 1456-1465.
18. S. Grimme, S. Ehrlich and L. Goerigk, 2011, **32**, 1456-1465.
19. V. Barone and M. Cossi, *The Journal of Physical Chemistry A*, 1998, **102**, 1995-2001.
20. F. Himo, *Journal of the American Chemical Society*, 2017, **139**, 6780-6786.
21. M. R. A. Blomberg, T. Borowski, F. Himo, R.-Z. Liao and P. E. M. Siegbahn, *Chemical Reviews*, 2014, **114**, 3601-3658.
22. R.-Z. Liao, J.-G. Yu and F. Himo, *Journal of Chemical Theory and Computation*, 2011, **7**, 1494-1501.
23. E. Bobyr, J. K. Lassila, H. I. Wiersma-Koch, T. D. Fenn, J. J. Lee, I. Nikolic-Hughes, K. O. Hodgson, D. C. Rees, B. Hedman and D. Herschlag, *J Mol Biol*, 2012, **415**, 102-117.
24. J. G. Zalatan, T. D. Fenn, A. T. Brunger and D. Herschlag, *Biochemistry*, 2006, **45**, 9788-9803.
25. S. Jonas, B. van Loo, M. Hyvonen and F. Hollfelder, *J Mol Biol*, 2008, **384**, 120-136.